SCIENCE ROBOTICS | RESEARCH ARTICLE

FIELD ROBOTS

Robotic locomotion through active and passive morphological adaptation in extreme outdoor environments

Max Polzin*, Qinghua Guan, Josie Hughes

Robotic locomotion has shown substantial advancements, yet robots still lack the versatility and agility shown by animals navigating complex terrains. This limits their applicability in complex environments where they could be highly beneficial. Unlike existing robots that rely on intricate perception systems to construct models of both themselves and their surroundings, a more bioinspired approach leverages reconfiguration to adapt a robot's morphology to its environment. Although interest in such multimodal, terrain-adaptive robots is increasing, their capacity for morphological reconfiguration often remains confined to specific body parts or comes at the expense of increased system complexity and reduced locomotion efficiency. Our study seeks to enhance robotic locomotion by developing robots that can actively reconfigure their morphology, altering their physical properties and leveraging their adaptability to navigate efficiently in diverse environments. We demonstrate how combining a compliant structure with morphological reconfiguration allowed a robot to transition between flat and spherical forms, enabling autonomous, multimodal locomotion—driving, rolling, and swimming—across complex terrains with minimal sensing. By actively reconfiguring its morphology to adapt physical properties for compliant interactions, the robot enhanced locomotion across rough, diverse environments. Leveraging its adaptability in different locomotion modes to navigate a 4.5-kilometer path across mountainous, aquatic, and urban terrains, the robot outperformed traditional and multimodal robots in terms of versatility, energy efficiency, and robustness. Developing versatile, energy-efficient, compliant robots capable of reconfiguring their morphology could substantially enhance autonomous navigation, opening up broader applications in unstructured environments, from environmental monitoring to disaster response and extraterrestrial exploration.

INTRODUCTION

The ability to autonomously traverse and locomote across terrains of varying gradients and to overcome obstacles or extreme surfaces remains a capability firmly associated with animals (*1*). Despite substantial advances in robotic locomotion and exploration, the versatility, efficiency, and autonomy of robots typically limit their application to a small range of preknown terrains or environmental niches. Through advances in robotic hardware, planning methods, and learning algorithms, robots are beginning to be able to operate in geometrically complex and dynamic environments (*2*, *3*). Yet, robots still lack the robustness and adaptability to respond to varied and challenging terrains as demonstrated by animals (*4*). However, the demand for robots of various sizes that can operate reliably under diverse and unpredictable environmental conditions is increasing. Robots with these capabilities can, for example, be used for biodiversity monitoring and surveying of sensitive ecosystems with minimal environmental effects across various habitats, including aquatic, terrestrial, and mountainous regions (*5*). For climate studies in extreme glacial or polar environments, robots with a small environmental footprint can explore confined spaces or cavities to gather essential data in challenging conditions (*6*). Lightweight, versatile, and robust field robots, despite their limited payload capacities, offer substantial benefits in areas like precision agriculture—where they reduce soil compression (*7*)—and space exploration—where their low weight makes them cheaper to transport (*8*). Amid increasingly severe climate events, there is a growing need for robots capable of providing support or rescue in the aftermath of landslides, earthquakes, and volcanic eruptions (*9*). In all of these scenarios, the terrain is complex, varied, and not always known in advance. By developing robots that can operate efficiently across a range of terrains, the use of robots can be extended to such applications, with the potential for substantial scientific, societal, and safety benefits (*10*, *11*).

One approach animals leverage to achieve versatility across terrains is the inclusion of compliance in their bodies (*12*). Compliance can be distributed in different structures and mechanisms (*13*). This has been observed in cockroaches, which can compress their bodies to navigate through tight spaces and absorb shocks (*14*); kangaroos, which store energy in their legs to enable an explosive hopping motion to overcome obstacles (*15*); or soft structured worms or octopuses, which can physically squeeze through narrow gaps or structures (*16*). These animals locally adapt to their environment for better navigation and for physical robustness against harsh or impactful interactions. Compliance can also enable physical reconfiguration, allowing animals to adapt their structural form to respond to a changing environment (*17*). A common example seen across nature is reconfiguration into a spherical form to provide robustness to the environment (Fig. 1A). Hedgehogs curl into a ball by tucking their bodies (*18*), armadillos assume a spherical form to be protected by their armored shell (*19*), and woodlice roll up into a ball for protection (*20*). Tardigrades, known for their ability to survive in the harshest conditions, protect their vital organs by contracting their bodies into a barrel-like shape (*21*). This reconfiguration can aid locomotion; the golden wheel spider (*Carparachne aureoflava*) changes into a spherical shape to facilitate energy-efficient locomotion on sand dunes (*22*). The phenomenon of adopting a spherical shape for mobility is also used by plants for dispersal across new

---

CREATE Lab, EPFL, Lausanne, Switzerland.
*Corresponding author. Email: max.polzin@epfl.ch

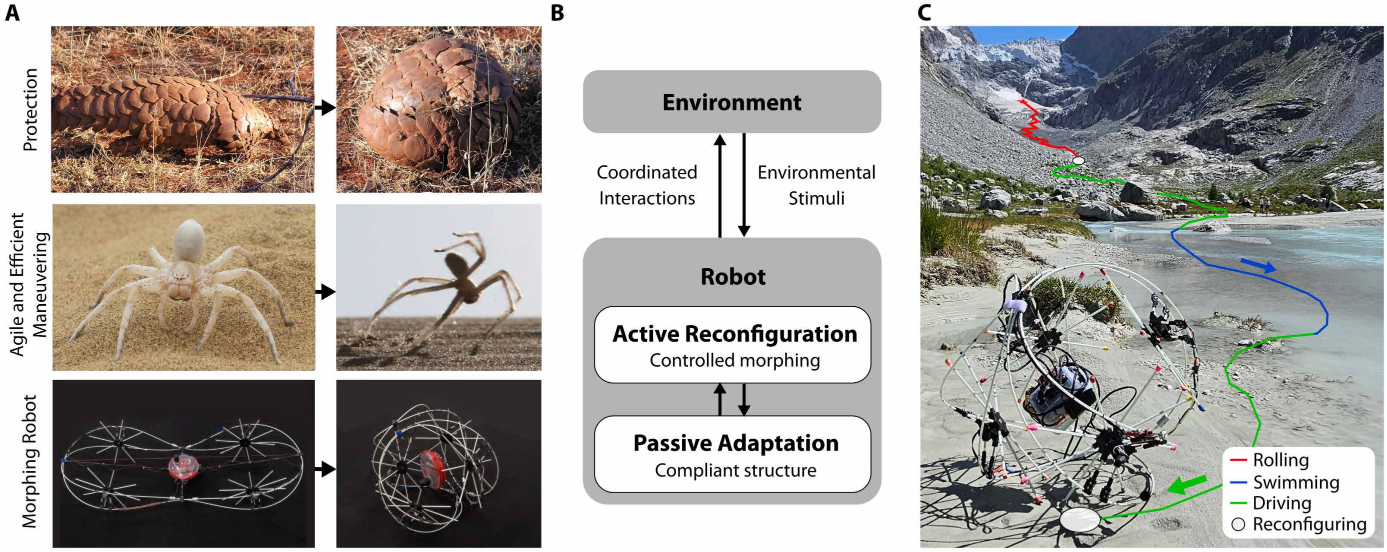

Fig. 1. Morphological reconfiguration and terrain-adaptive locomotion. (**A**) Reconfiguration capabilities of animals from locomotion to spherical shapes and the GOAT robot with similar capabilities. (**B**) The role of active reconfiguration for adapting to the environment and altering the passive properties of the robot. (**C**) Image of the robot in the ball configuration demonstrating the types of terrain that can be covered and the different modalities of locomotion that can achieve this.

habitats (*23*). Tumbleweeds, for instance, of the resurrection plant (*Selaginella lepidophylla*), use this form to be carried by the wind to colonize distant environments (*24*). Active morphological reconfiguration is an evolved response that has occurred across organisms of different sizes and structures and for different environmental niches. In all of these cases, these organisms use the compliance of their bodies to actively reconfigure their shapes in response to environmental stimuli. This reconfiguration leads to a substantial change in the passive properties of these organisms' bodies and provides advantageous interactions with their environment.

Active reconfiguration has been explored as a means of expanding robotic capabilities. Typically demonstrated in rigid robots, reconfiguration can enable switching between locomotion modalities such as flying or locomoting (*25*, *26*), enabling wall climbing (*27*) and navigation in varied terrain (*28*). Reconfiguration can also be localized within the body, for example, in wheels that transform to overcome obstacles (*29*–*33*) or that can be folded to save space (*34*). More modular, origami-inspired approaches rearrange or combine modules to locomote (*35*). However, the modularity can make dynamic adaptation challenging (*36*). Tensegrity robots (*37*) and truss-style morphing enable larger, meter-scale morphing robots (*38*), but the speeds of motion are typically low. Embedding compliance into reconfigurable robots has been shown to be advantageous and can enable locomotion across land and water (*39*, *40*). Examples include reconfigurable soft flippers and wheels on the compliant-legged hexapod robot RHeX (*41*–*43*), compliant augmentation of a rover (*44*), and adaptive morphogenesis for flipper-leg repurposing in a turtle-inspired robot (*45*). Many compliant reconfigurable locomotion designs also take direct inspiration from animals (*46*). Robots inspired by the golden wheel spider move by cartwheeling to traverse sand dunes (*47*, *48*); others autonomously adapt their shape to confined spaces to overcome obstacles (*49*) or release energy stored in their frame to jump and overcome obstacles (*50*). This body of work validates the advantages of compliant reconfigurable robots. However, changes to the underlying passive properties and morphology are often limited such that the range of environments in which these robots can operate robustly remains low.

Drawing inspiration from the concept of reconfiguration observed in animals and plants (Fig. 1A), we propose that active reconfiguration of a robot must lead to a change in its underlying passive properties. We present a robot in which the active reconfiguration of the robot's morphology enables control over the robot's passive properties and the resulting autonomous behavior (Fig. 1B and Movie 1).

This robot was fabricated from elastic fiberglass rods, tethers, and electrically driven winches and wheels to form a meter-scale compliant robot. The robot structure leverages lens-like structures to control torsional stiffness, enabling the structure to reconfigure from a flat rover for driving to a spherical form with its wheels tucked inside. This was achieved by designing the energetics of the structure appropriately and ensuring that the reconfiguration space avoids undesirable twisting or buckling modes. The continuous reconfiguration space of the robot enables rapid online adaptation for different modes of locomotion, including driving, swimming, and rolling. It enables our robot, termed GOAT (Good Over All Terrains), to traverse complex terrains, including mountainous, aquatic, and urban environments. The robot's passive properties vary from highly compliant and adaptive in its flat configuration, enabling locomotion through adaptation to the terrain, to elastic and robust in the spherical configuration, resulting in rolling, falling, and dropping behaviors. By adapting its configuration and passive properties to the environment, the robot shows greater physical robustness and simplifies autonomy, enabling it to navigate autonomously with only positional information.

To demonstrate the potential of active morphological reconfiguration combined with compliance, we present an evaluation of both the active and passive capabilities of our robot. This evaluation highlights the robot's capacity for autonomous behavior with minimal perception systems, relying instead on its passive capabilities to interact with and respond to its surroundings (Fig. 1C).

CREDIT: PANGOLIN (68, 69); SPIDERS (70, 71)

Movie 1. Summary video of the GOAT. Overview of the robot and demonstration of its capabilities for active-passive morphological reconfiguration and terrain-adaptive locomotion in extreme outdoor environments.

Our experiments showcase the robot's proficiency by demonstrating it autonomously traversing more than 4 km of varied and challenging terrains, including snow, rocks, water, and ice. By using low-level decision-making and strategically choosing its morphological configurations, the robot can improve its locomotion efficiency and adeptness in navigating complex landscapes. This approach of incorporating active and passive reconfiguration demonstrates how environmental adaptation can minimize computational demands for path planning and enhance efficiency over challenging and extreme terrains.

RESULTS

Reconfigurable compliant design

For the robot to reconfigure from a wheeled driving configuration into a spherical form, its frame had to deform three-dimensionally, assume a spherical shape, and avoid twisting or buckling. Furthermore, the design of the frame had to support reconfiguration in a way that allowed control of the orientation and tucking inward of the wheels to form a fully spherical shape. To enable this reconfiguration, the robot's frame was fabricated from two elastic fiberglass rings, which were connected to form a circular structure with a woven pattern. Tendons span orthogonally across the frame and were connected to electric winches at the floating payload in the center of the robot. There was a trade-off between frame compliance and payload capacity; higher stiffness supported heavier payloads but reduced compliance and increased the energy needed for morphing. The selected frame stiffness represented a compromise between these factors to support the 1.8-kg payload and enable robust locomotion and efficient morphing. Figure 2A shows the robot's design, including its four rimless wheels, in its open form and its reconfiguration capabilities. By controlling the winch-driven tendons in a given actuation sequence, the robot was able to alter its shape in plane for efficient and robust locomotion and out of plane to compactly reconfigure into a sphere. In its spherical configuration, the payload was centrally suspended within the robot, and the wheels were folded inward toward the center of the robot.

The woven pattern of the elastic rods that form the robot's frame was crucial for achieving stable and unambiguous reconfiguration. Using finite element analysis, the deformation profiles, stability, and tendon forces were predicted for different frame designs. To model the elastic rods that undergo large deformation, we developed a modeling method on the basis of absolute nodal coordinates formulation (ANCF) (*51*) that offered accurate prediction of the three-dimensional (3D) deformation and was computationally efficient. Alongside the 3D deformation, our adapted ANCF methods enabled estimation of flexural rigidity, torsional rigidity, and elastic potential energy. This estimation enabled the nominal energy density distributed throughout the frame to be computed, which indicated the extent of the energy stored in different configurations.

Using this analysis and the estimation of the deformation, we determined the effects of morphing capabilities for different frame designs to demonstrate the importance of the woven lens shape of the frame. For the same winch placement and tendon routing, but with a ring made of a single rod, the frame structure exhibited stable in-plane and 3D, out-of-plane reconfiguration at low tendon forces (Fig. 2B). However, because the rod was free to rotate around its central axis, the wheel orientation was not constrained. Therefore, the wheels were not folded away when reconfiguring into a sphere. To constrain the wheel orientation during reconfiguration, the frame could be designed as a band structure composed of two fiberglass rings rigidly connected with constant separation. This configuration demanded considerably higher tendon forces for reconfiguration. In addition, during out-of-plane deformation, this band structure tended to become unstable, leading to a flipping of the band, which obstructed complete reconfiguration.

The frame of our robot was constructed from two fiberglass rings, interconnected to form a pattern of four symmetric, convex lenses between them. The wheels were positioned at the center of these lenses. During reconfiguration, this structure required similarly low tendon forces as observed in the single ring structure (Fig. 2B, iii). In contrast with the band structure, it allowed the frame to fully and unambiguously reconfigure into a sphere. In addition, the orientation of the wheels was constrained, ensuring that as the frame folded into a spherical shape, the wheels faced toward the robot's center. The frame of the robot allowed for continuous reconfiguration, with the possible reconfiguration space defined by the lengths of the two winch-operated tendons (movie S1). Certain tendon configurations in this reconfiguration space could lead to a twisting of the frame. By examining the torsion stiffness of the pivot point of the reconfiguring frame, we identified the likelihood of unconstrained, unstable, and undesired twisting motions (*52*). This metric was computed systematically across the reconfiguration space (Fig. 2C). When torsion stiffness was below zero, these structures showed unwanted and unstable twisting behaviors.

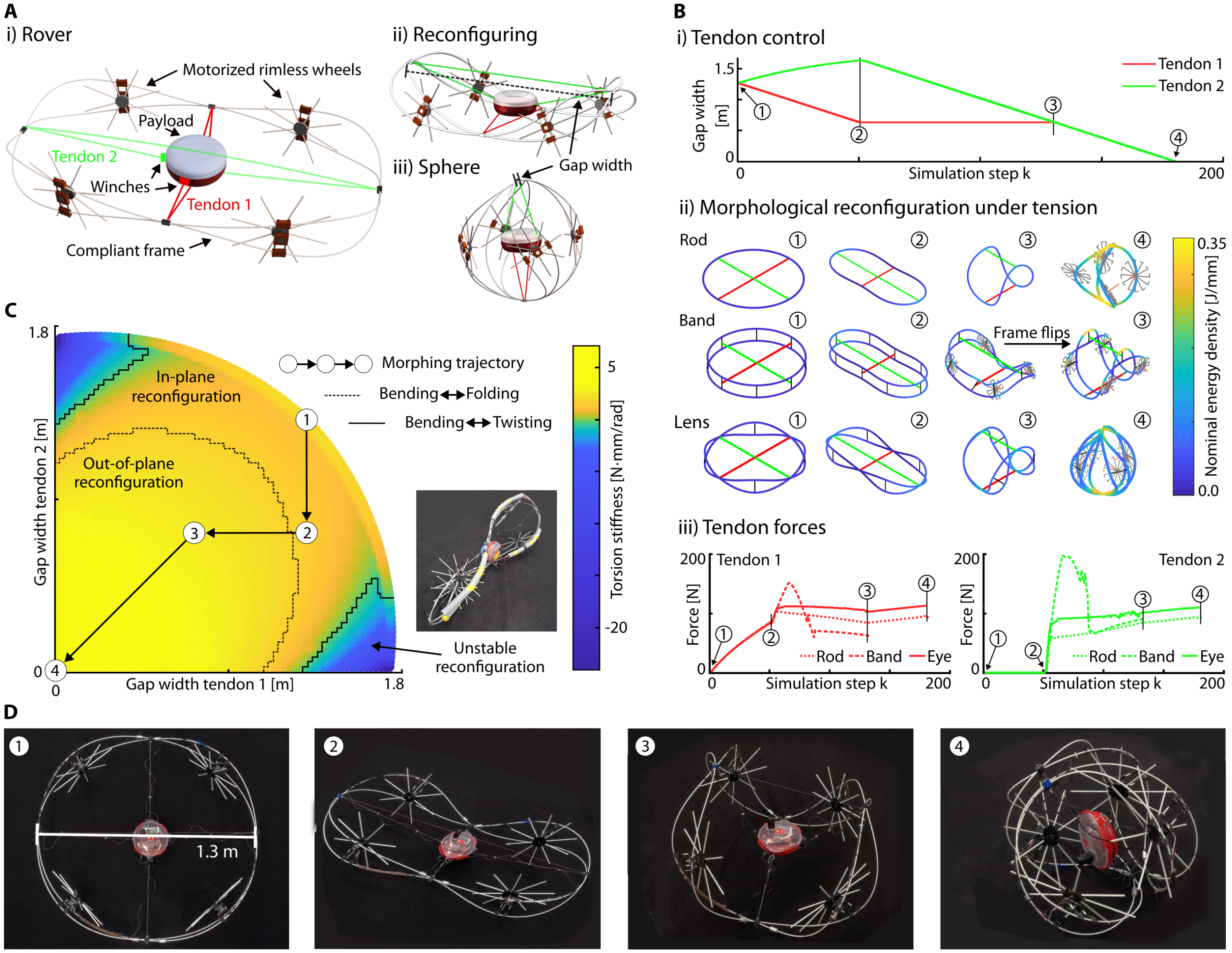

Fig. 2. Robot design and configuration analysis. (**A**) Compliant frame with four rimless wheels and actuated tendons enabling rover configuration (i) and reconfiguring (ii) to a sphere (iii) through tendon length adjustments. (**B**) For the tendon control sequence in (i), frames made from a single rod, a band, and our robot's lens pattern, experience morphological reconfiguration (ii) whereby different tendon forces occur (iii). (**C**) Morphological configuration space showing reconfiguration regions (bending, folding, and twisting), with the *x* and *y* axes representing the tendon gap indicated in (A). The black line illustrates a tendon control sequence to reconfigure from state 1 (circular) to 2 (rover), 3 (reconfiguring), and 4 (sphere). (**D**) Time-lapse sequence of the robot's progression through configuration states 1 (circular), 2 (rover), 3 (reconfiguring), and 4 (sphere). Labels 1 to 4 correspond to the same configurations in (B) (lens), (C), and (D).

Within the "safe" reconfiguration space, there existed three regions. First, in the outer region of the tendon reconfiguration space, in-plane reconfiguration occurred. This reflected a change from a circular shape to a rover shape suitable for driving or one that fits through gaps (Fig. 2D, markers 1 and 2). Second, when the tendon lengths were further reduced, out-of-plane reconfiguration occurred. The wheels of the robot lifted off the ground and folded inward when the frame took on a spherical shape. This continued until the frame was fully reconfigured into a spherical shape. Last, there was the unstable "twisting" region, which had to be avoided. When switching between different configurations, a path of tendon configurations had to be chosen that avoided unstable regions. In Fig. 2C, an exemplary path (1 to 4) for reconfiguring from a circular to rover to spherical shape is indicated. Figure 2D shows an exemplary time-lapse sequence of the robot's reconfiguration, following the control signals detailed in Fig. 2B and the morphological reconfiguration path outlined in Fig. 2C. Last, when keeping the total length of both tendons constant, the payload suspended in the robot's center could be moved independently of the robot's frame. This arrangement enabled the initiation of a rolling motion by moving the center of mass of the robot without altering the overall configuration.

Passive adaptation

The robot's two main configurations, namely, the spherical and rover shapes, allowed different forms of locomotion. The robot leveraged each configuration's specific passive properties to be resilient and robust in different environments (movie S2). In this section, we illustrate these passive properties and how they are key to enabling autonomous navigation in the robot's two main configurations.

Flat configuration

In its flat configuration, the robot leveraged compliance in its frame to overcome obstacles. The robot overcame obstacles that were 14% higher than its center of mass with a success rate of 38% (Fig. 3A). Further, the compliance in the frame aided in traversing narrow gaps. The robot passively compressed to fit through openings smaller than its width, successfully passing through them if it had adequate traction and forward momentum (Fig. 3B and movie S3). To evaluate this ability, the success rate for the robot passing through gaps of reducing size was calculated. This demonstrated that the robot could successfully squeeze through gaps more than 10% smaller than its starting frame width.

Autonomous driving

In its rover configuration, the robot's compliant frame enabled it to robustly maneuver in diverse environments, overcoming obstacles like steps and driving on varying slopes and surfaces. This meant that the robot did not require detailed terrain analysis or complex path planning but could leverage onboard state estimation to navigate between waypoints. Using measurements from onboard sensors [global navigation satellite system (GNSS)–based position

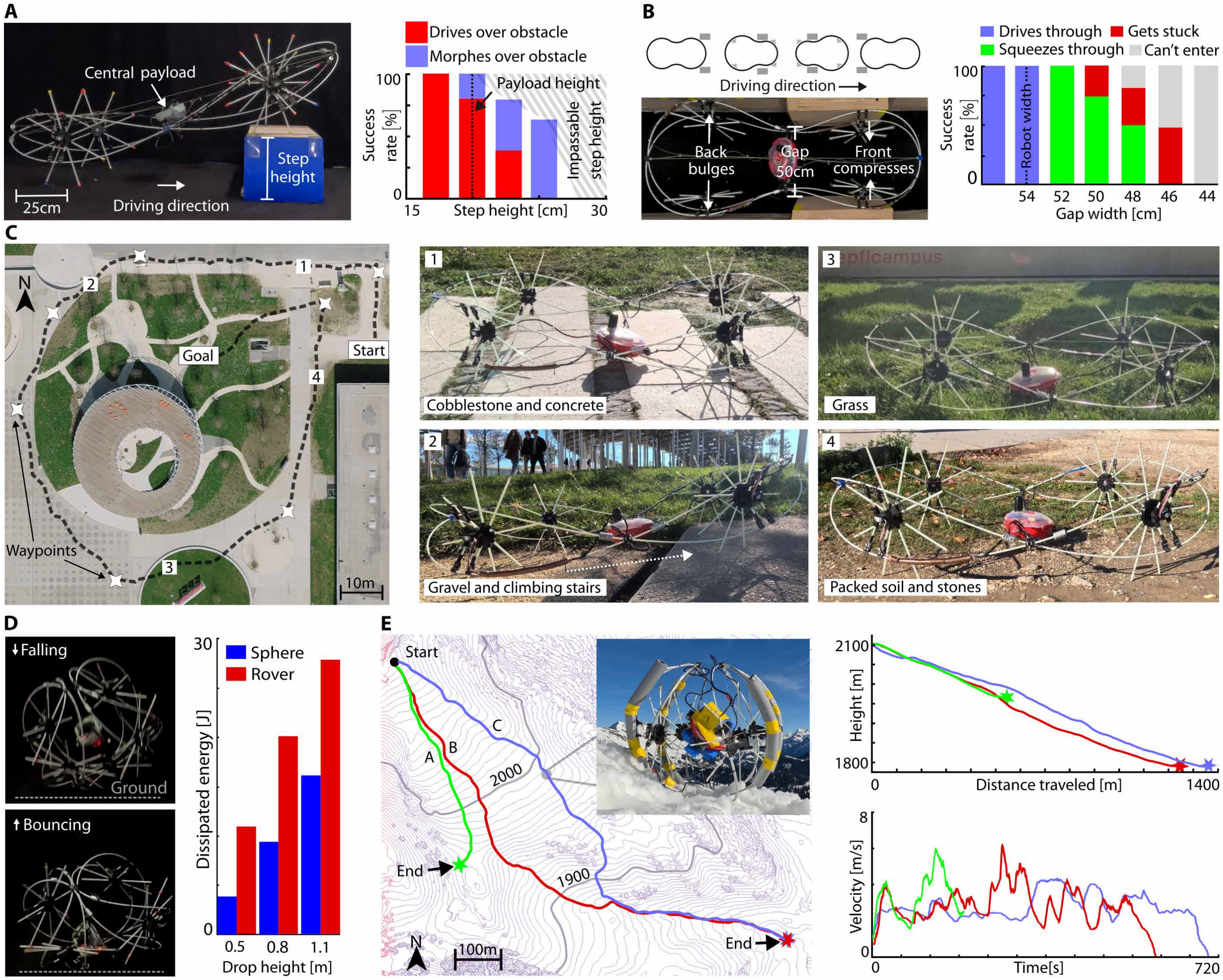

Fig. 3. Locomotion leveraging passive adaptation. (**A**) The robot drove over steps (17 to 26 cm high). When stuck on a step and reconfiguring, the robot can overcome higher obstacles. Its success rate to drive, respectively, morph over steps is shown. (**B**) The robot was commanded through small gaps (56 to 44 cm wide). For gaps narrower than the robot (54 cm), the compliant frame deforms and enables squeezing through. The success rate to get through gaps is shown. (**C**) Autonomously driven path around EPFL, Lausanne, Switzerland, guided by predefined waypoints. The numbered markers and accompanying images showcase the variety of terrains and structures encountered. (**D**) The pictures show the robot in spherical configuration dissipating impact energy through elastic deformation and bouncing. The dissipated energy of two configurations (rover and sphere) is shown for the robot being dropped from three different heights. (**E**) Three rolling trajectories for the robot in its spherical configuration from the same starting point on a peak. Contour lines indicate regions of equal altitude. The inset photo shows the rolling robot, highlighting the snowy mountainous terrain.

sensor, inertial measurement unit (IMU)] to provide a robust estimation of its location and heading, the rover autonomously followed a set of predefined waypoints, where a low-level path-following controller enabled navigation between them. This enabled the robot to autonomously traverse complex and varied terrains, as shown by the 307-m path followed in Fig. 3C, where the robot followed eight predefined waypoints. The low-level autonomy and physical compliance of the robot enabled it to traverse over various challenging terrains with minimal planning. Furthermore, the planning and low-level control algorithms did not need to be specific for different terrains or topographies.

Spherical configuration

The spherical configuration of the robot enabled it to cover diverse and challenging terrains, which could include substantial drops, for example, from cliffs. Because the payload was suspended centrally within the frame, the spherical configuration not only provided physical robustness to the robot frame but also protected the easily damaged payload of the robot. When the robot was dropped from a height, the frame elastically absorbed the impact forces and gradually dissipated them. Initially, it deformed before the elastic deformation in the frame led to the robot bouncing and restoring its initial configuration. This process effectively protected both the payload and the frame from damage. To demonstrate the effectiveness of the spherical configuration, we compared the energy that was dissipated upon impact by the robot in the spherical configuration with that in the flat rover configuration. This energy was measured by observing the rebound height of the robot after drops from varying heights using motion capture. In the rover configuration, impact energy was dissipated by both the robot's frame and the payload upon hitting the ground. In contrast, in the spherical configuration, a portion of the kinetic energy was converted into elastic deformation upon impact, resulting in substantially less energy being absorbed by the frame and none by the payload. This effectively shielded the payload, given that all the energy was dissipated by the frame (see Fig. 3D). Although the impact energy to be dissipated increased linearly with drop height, the spherical configuration's elastic deformation reduced the total energy that had to be dissipated upon impact by the frame by approximately half compared with the rover configuration (Fig. 3D). The robot's capacity for efficient and gradual energy dissipation in the spherical configuration enabled the robot's frame to undergo substantial drops when rolling without damage, including drops of more than 10 m, as visualized in fig. S9. When planning a route for the robot in this configuration, this meant that extreme features such as cliffs or drops did not need to be avoided but could be leveraged to offer an optimally efficient path.

Rolling autonomy

This physical robustness allowed the spherical form to be leveraged for rolling. The robot could self-instigate rolling, as described in the spherical reconfiguration section. Once rolling, it could follow the surrounding environmental gradient autonomously without any control inputs. When leveraging this functionality during navigation, we refer to it as environmental computation. An exemplary visualization is shown in movie S4. Although the path followed depends on the terrain and topology, substantial distances were traveled. The rolling capabilities were tested in a snow-covered mountain environment (Villars-sur-Ollon, Switzerland). Rolling was instigated three times in the same location, and the rolled trajectories were recorded for three repeats (Fig. 3E). When rolling, the robot reached velocities up to 6 m/s. In two instances, the robot covered a distance of 1.4 km. During the top part, when rolling along a mountain ridge, the trajectories diverged but converged to the same end point because of the topographic features of the surrounding terrain. It was not intended for the robot to end up in the same location for the rolled trajectories but to capture the possible variability when rolling in a complex terrain. In another case, the robot rolled to a local topographic minimum and ended in another location. Thus, when rolling, the robot could follow a gradient and terrain-driven path, which could be beneficial for rapidly and efficiently descending slopes.

Active reconfiguration

In addition to the robot leveraging its passive properties in different configurations to simplify autonomy and providing different means of locomotion, the robot could also leverage active reconfiguration to achieve additional modalities of locomotion. Active reconfiguration—such as adjusting its aspect ratio for optimized speed and turning or curling up and redistributing its payload to facilitate rolling—allowed it to adapt to various environments. Integrating these capabilities into autonomous navigation strategies enhanced the robot's adaptability, speed, and energy efficiency on complex terrains.

Flat reconfiguration

When in flat configuration, the wheels of the robot were in contact with the ground, and it could drive. Within this configuration, the lengths of the two orthogonal tendons, l_1 and l_2, were varied to change the aspect ratio of the robot from a circle (aspect ratio, $r = l_1 / l_2 = 1$) to a narrow figure-of-eight form (aspect ratio, $r = 6.5$) as shown in Fig. 4A. The robot's aspect ratio affected the achievable speed and drift when driving and turning. This was evaluated by recording the trajectories for forward driving and turning when the robot was in different aspect ratios. The fastest speed (1.4 m/s) was achieved when the aspect ratio was such that the wheels were aligned with the direction of travel, for an aspect ratio between 2 and 3 (Fig. 4B). The speed then decreased with the two extremes of aspect ratios. The positional error, or percentage drift when moving forward, showed a similar relationship, with the best performance, meaning the lowest positional error, seen when the wheels were aligned with the direction of travel ($r = 2.2$). When turning, the angular velocity was highest when $r = 1$ and the robot was closest to a circle (Fig. 4C). As the ratio increased, it was increasingly difficult for the robot to turn. Eventually, turning became impossible when the wheels were turned inward for $r = 6.4$. The turning ratio similarly increased with aspect ratio. A ratio of 1.4 to 2.2 offered a compromise in terms of forward speed and ease of turning. However, depending on the path of the robot and the turning radius required, morphing within the flat configuration could aid in speed, controllability, and maneuverability of the robot.

Spherical reconfiguration

When in the spherical configuration, the payload of the robot was suspended on the tendons within the robot. By maintaining the same total tendon length, but varying the ratio between tendons 1 and 2, the payload could be moved along the tendons besides maintaining the identical spherical configuration of the robot. Because the payload was substantial with respect to the lightweight frame, this could be used to move the center of mass outside the support polygon of the robot and instigate rolling motion (Fig. 4D and movie S5). Using the encoders on the winches, this operation was automated and took less than 15 s. Using motion capture, the rolling motion of the sphere was recorded for repeated trials on flat ground. First, initial perturbations were observed. After reaching a "tipping"

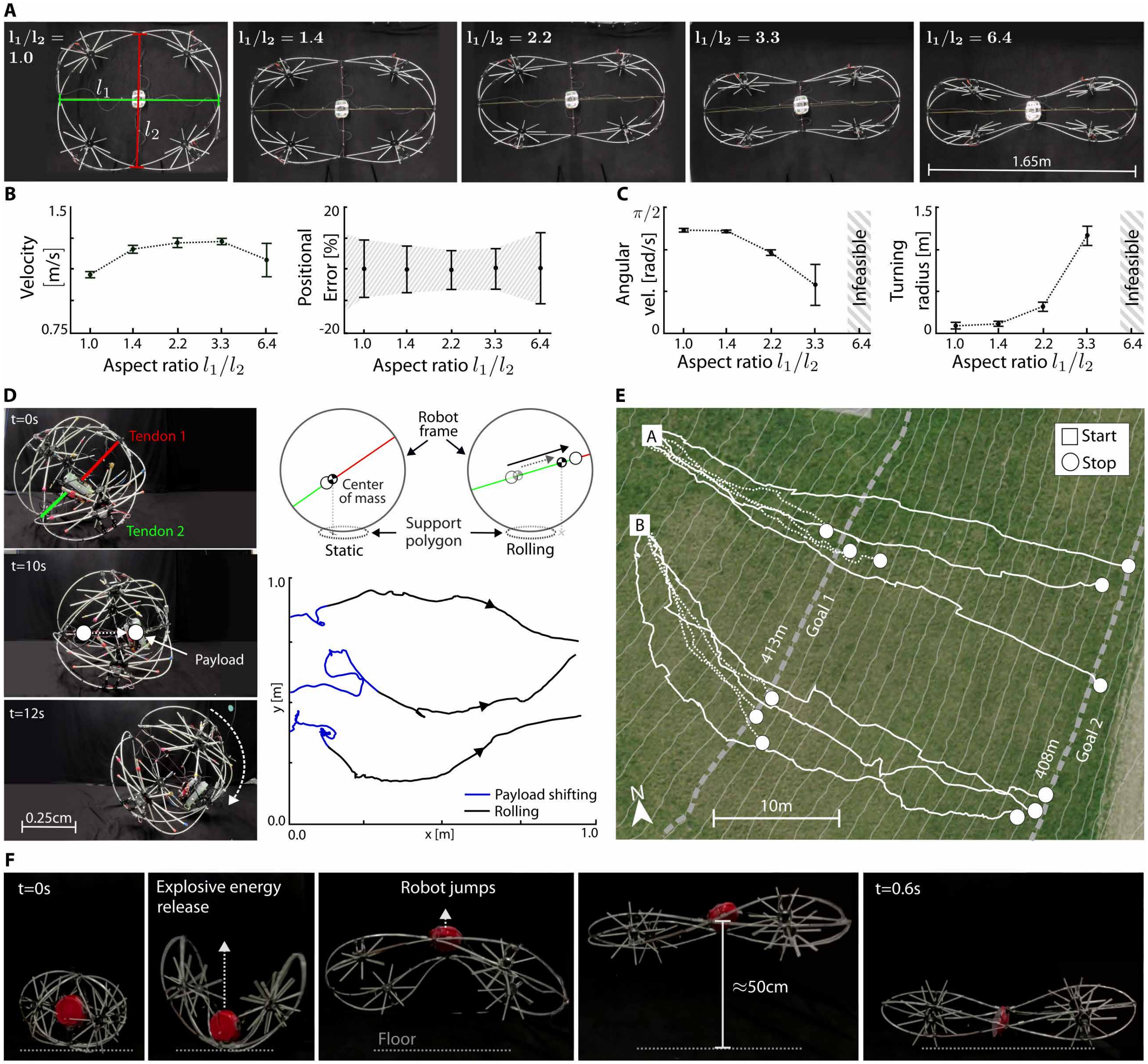

Fig. 4. Active reconfiguration for motion control. (**A**) The ratio of tendons 1 and 2 allows reconfiguration of the robot's aspect ratio. Pictures show a time-lapse sequence of the robot reconfiguring from a circle, $l_1 / l_2 = 1.0$, to a figure eight, $l_1 / l_2 = 6.4$. (**B**) The aspect ratio affects driving velocity and odometry accuracy. The mean and SD for velocity and positional error for five trials per aspect ratio are shown. (**C**) The robot's turning speed and radius are linked to its aspect ratio. The mean and SD for five trials per aspect ratio are shown. (**D**) The winch-driven tendons can be used to move the payload and, hence, the center of mass to initiate rolling on flat ground. The motion of the sphere when rolling is shown for three repeats as measured by motion capture with markers tracking the payload. (**E**) The robot rolled from two starting positions, A and B, and automatically reconfigured from sphere to rover to stop at two different targets, goals 1 and 2. (**F**) Time-lapse images showing the motion of the robot when a tendon is promptly released.

point, the robot rolled smoothly (Fig. 4D). The direction of rolling was determined by the motion of the payload. Rolled distance and path were approximately constant and corresponded to half of the circumference of the robot. The ability to shift its center of mass enabled the robot to automatically initiate rolling on flat or close-to-flat slopes.

Reconfiguration from sphere to rover

After instigating rolling, reconfiguring to a rover enabled control over the distance traveled (movie S6). To illustrate the repeatability of this process, for two different starting points on a grassy slope, reconfiguration from sphere to rover was instigated after a given time to reach two target goal positions. Figure 4E shows the rolled paths and the stopping locations for the goal distances. Although there were some variations, a repeatability of ±2 m was observed. The robot's ability to actively stop rolling through morphological reconfiguration enabled the integration of controlled rolling as a locomotion modality into autonomous navigation strategies.

Explosive reconfiguration from sphere to rover

Transitioning from spherical to rover shape using the robot's electric winches enabled controlled stopping; however, this process took some time, limiting the robot's response time to a stopping signal. When in the spherical configuration, the fiberglass rods stored elastic potential energy, applied by the winches. Leveraging clutches on the robot's winches enabled a rapid release of the tendons, and the stored energy could be released explosively (movie S7). This rapid release of energy when the robot was in a spherical configuration led to a jumping behavior of the robot, where heights of 0.5 m could be reached in less than 0.3 s (Fig. 4F). This offered an effective maneuver to overcome obstacles, escape challenging situations, or come to a more immediate halt.

Navigation leveraging reconfiguration

The robot's capacity for active morphological reconfiguration enabled the combination of its different locomotion modalities for efficient autonomous navigation. Three navigation strategies, schematically depicted in Fig. 5A, were considered as a means of reaching a target location mid-hill: (i) driving directly to the target; (ii) rolling until passively stopping followed by driving to the target; and (iii) rolling, actively reconfiguring to rover when at the same height as the goal, and driving to the goal. Our path planning algorithm did not have prior information about the surrounding terrain available. A flow chart visualizing the decision-making for autonomous reconfiguration for each of the above navigation strategies is shown in fig. S5. The navigation strategies were evaluated on the basis of the robot's ability to reach a target location on a grassy slope (Fig. 5B). For each strategy, metrics including the path taken, time elapsed, and energy consumption were measured (Fig. 5C). Driving directly to the target resulted in the shortest overall path of 22 m. In comparison, rolling down until naturally stopping and consecutively driving uphill toward the goal resulted in a path 2.5 times longer than driving directly and required more time and energy than the other strategies. The surplus of energy was required because driving uphill consumes more energy than driving downhill. Rolling, actively stopping by reconfiguring to rover, and driving toward the goal took less time than the other strategies despite the distance traveled being slightly larger than driving directly toward the goal. Critically, we observed that the combination of rolling, active reconfiguration, and driving reduced the energy consumption by a factor of four in comparison with driving directly. This demonstrated how the robot's capacity for active reconfiguration allowed it to leverage the advantages of each configuration to increase navigation efficiency.

Real-world deployment

By leveraging the robot's reconfiguration capabilities appropriately, the robot could operate in and transition between diverse natural environments. Two example real-world deployment scenarios are shown, demonstrating how morphological reconfiguration facilitates seamless access and maneuverability in various environmental contexts.

Multiterrain operation: Land, water, and rocks

Transitioning from locomotion on land to surface swimming in water and traversing rocky terrain was challenging because of the different locomotion modes required and the obstacles present. The robot's ability to operate in these environments was tested on the lakefront of Lake Geneva in Lausanne, Switzerland, with a sandy, stony beach cluttered with flotsam and a surrounding wall of boulders. The robot started driving on the beach, heading to an initial waypoint in the water, and then returning to the beach and finally reaching the goal position by traversing a wall of boulders. We combined autonomous and teleoperated operation. Using the same controllers for path following, the robot could automatically transition from the beach to the lake (Fig. 6A and movie S8). Leveraging its wheels to generate thrust, the robot could swim and reach a specified waypoint. In water, the robot showed maneuverability leveraging its four-wheel differential drive. Its velocity in water was constant at 0.5 m/s, a speed comparable to that of locomotion on land. However, the power consumption when swimming was 56% lower and far more consistent. The robot could autonomously transition from water to land, leveraging its open wheel structure. The third terrain to traverse was a wall of boulders. Although the robot could gain some traction to move over and among the boulders, it got stuck. To get unstuck, overcome the boulders, and return to the lake, the robot was commanded to automatically take on its spherical shape. It rolled back into the lake (Fig. 6A). Once again floating, the robot switched back to its rover configuration and swam to the final goal

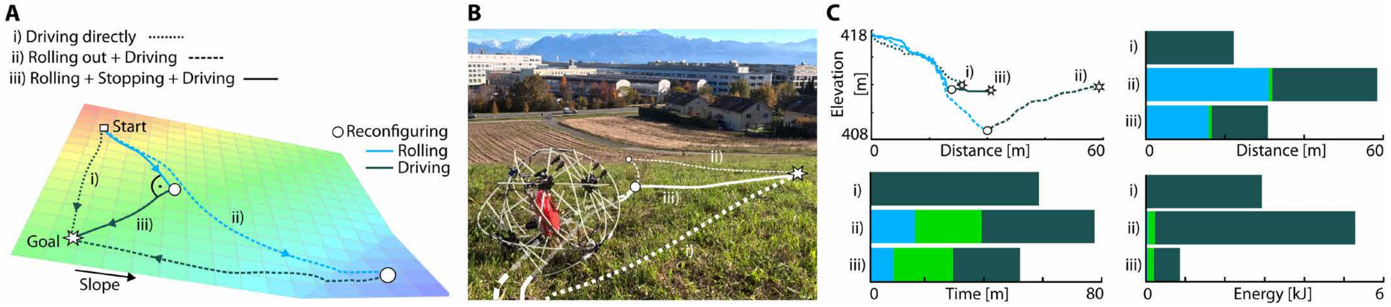

Fig. 5. Autonomous navigation strategies. (**A**) Schematic visualization of three strategies for autonomous navigation: (i) direct driving; (ii) rolling, passively stopping, and driving; and (iii) rolling, actively stopping through reconfiguration, and then driving toward the goal. (**B**) An image of the robot in the experimental environment. The starting point and the trajectories across the sloped terrain for the different navigation strategies (i to iii) are illustrated. (**C**) Comparative data analysis showing the elevation change, distance traveled, time passed, and energy consumed during driving (dark teal), reconfiguring (green), and rolling (blue) for each navigation strategy (i to iii).

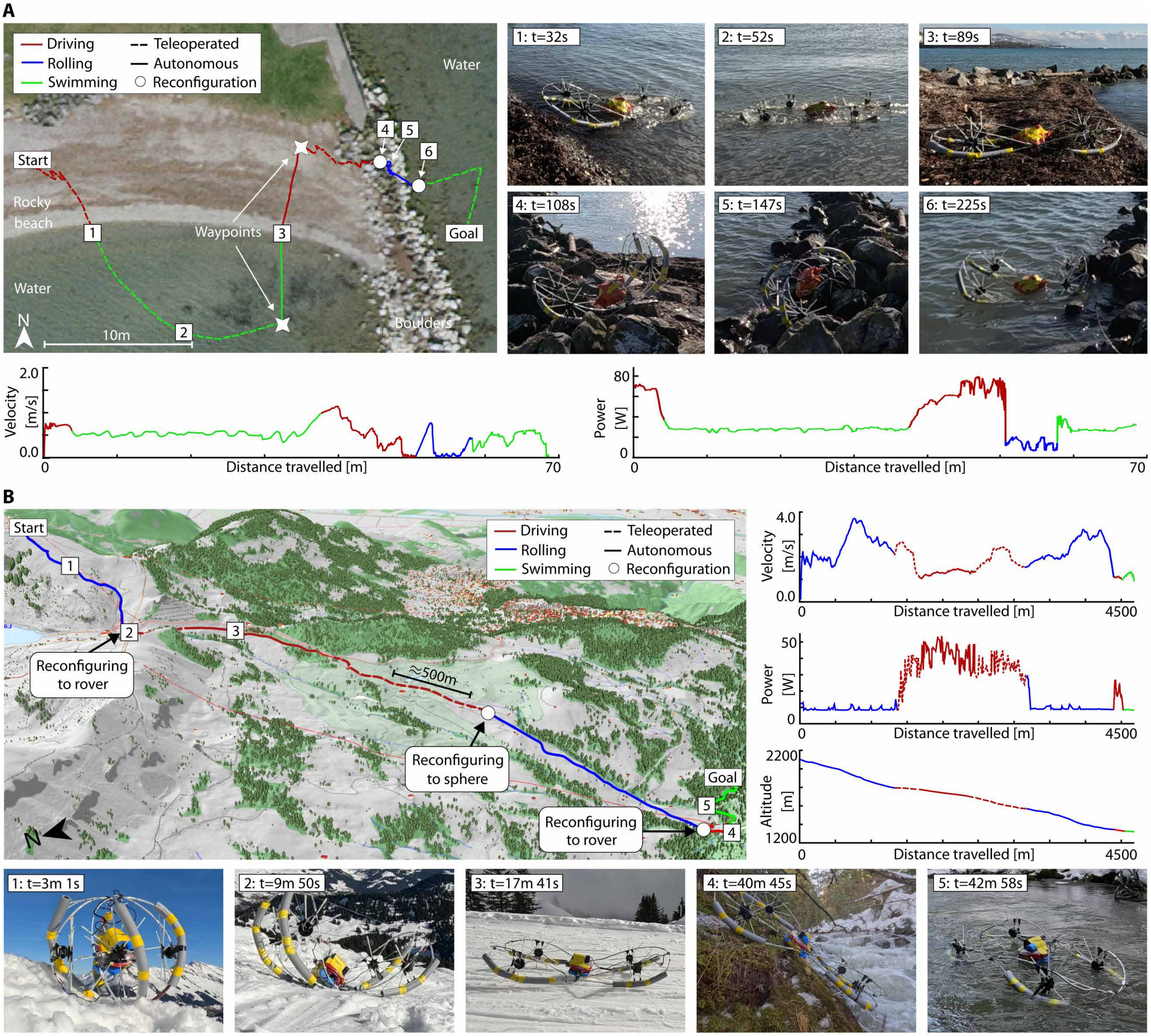

Fig. 6. Multimodal locomotion experiments in extreme outdoor environments. (**A**) Demonstration and evaluation of the robot using active morphological reconfiguration to follow a path over a flotsam-cluttered beach, through water, and across boulders. Pictures show the robot at different points on its path. The velocity profile and power consumption were evaluated in relation to the distance traveled. (**B**) Multimodal navigation in a mountainous environment, with the path taken shown and the velocity, altitude profile, and power consumption evaluated in relation to the distance traveled. Pictures highlight the robot operating in different locomotion modalities (images 1, 3, and 5), reconfiguring from sphere to rover (image 2), and transitioning between environments (image 4).

location in the lake. The total distance traveled was 70 m whereby the robot covered 40 m swimming, 25 m driving, and 5 m rolling. The robot's compliance facilitated seamless navigation across varied terrains and smooth transitions between them because its capacity for active morphological reconfiguration allowed it to effectively overcome obstacles.

Operation in a mountainous environment

The robot was deployed in the varied mountainous landscape around Villars-sur-Ollon (Vaud, Switzerland), tasked with traversing snow-covered slopes, rugged mountains, streams, and rivers to reach a destination 4.5 km away from its starting location (Fig. 6B). This scenario required the robot to engage in driving, rolling, and swimming locomotion. The robot was partially teleoperated and partially autonomous on this path, operated with a single battery charge, and changed its configuration three times. For the first section of the path, a steep slope, the robot rolled down the slope in its spherical configuration, reaching speeds up to 4 m/s; the ability to follow the environment enabled a meaningful path to be autonomously followed by the robot. During this 10 min of rolling, the only energy consumed was by the robot's onboard computer, which captured data and ran the robot's software stack. This offered a reduction by almost 90% in power consumption compared with its driving configuration. In the subsequent 1.8-km-long flat section, the robot automatically transitioned into its rover configuration and autonomously followed a series of commanded waypoints. The robot drove up to 2.3 m/s and consumed on average 39 W. When reaching a second steeper part, the robot was commanded to reconfigure back into a sphere and leveraged its energy-efficient rolling mode. During this experiment, more than 4.5 km of distance was covered, and around 1000 m of height was descended. Over this 4.5-km traverse, the robot did not experience any failures, nor did it get irrecoverably stuck. Last, a river flow was leveraged to reach the final destination. The robot reconfigured into a rover to enter the stream, after which it leveraged the river flow, requiring minimal power to reach its goal location. Through reconfiguring, the robot leveraged the environment for control and minimized energy consumption.

Comparative metrics

The performance of the robot was compared with that of other robots designated for operating across diverse outdoor environments using several metrics as presented in Table 1. We first focused on key metrics for terrestrial locomotion. These included efficiency metrics, such as the cost of transport (CoT), total weight, and distance per charge, and performance metrics that reflected outdoor behavior, including the maximum slope that could be ascended, maximum drop height, maximum velocity on flat ground, and the payload capacity. Further, we compared performance and efficiency metrics for locomotion in aquatic environments, such as distance per charge, CoT, and maximum velocity where possible. The energy efficiency of GOAT, as represented by its CoT, was higher when compared with that of other robots for terrestrial locomotion. The rolling locomotion mode, when rolling downhill, showcased GOAT's efficiency, being 10 times more efficient than ANYmal (*53*), 26 times more efficient than M4 (*28*), and 100 times more efficient than ART (*45*). In its driving configuration, the GOAT's CoT was approximately 30% lower than that of ANYmal. Weighing only about $^{1}/_{10}$ of ANYmal, the GOAT was designed for operational needs with a reduced payload capacity. Unlike ANYmal, the GOAT could be easily transported in a backpack (see fig. S14). We included ANYmal in the comparative metrics because it is one of the few robots for which comprehensive outdoor test data over long distances in rugged, varied terrain have been reported in the literature (*3*). In aquatic environments, the GOAT robot's CoT was 3.3 times lower than ART's most efficient mode. ANYmal and M4 were infeasible for aquatic locomotion. In terms of distance covered on a single charge, the GOAT traveled 4.5 km, similar to the ANYmal robot covering 2.2 km and M4's estimated maximum range of 2.4 km. The GOAT robot could swim up to 2 km per charge. For ART, no maximum range was reported because it was operated tethered. For terrestrial locomotion, the GOAT robot reached a competitive maximum slope ascending capability of 33° compared with ANYmal's 21° and the thruster-assisted M4's 45°. It achieved a maximum driving velocity of 2.4 m/s, twice that of ANYmal's reported 1.2 m/s, and was robust to drops exceeding 10 m. The GOAT robot's maximum swimming velocity of 1.2 m/s was substantially higher than ART's (0.09 m/s). Diverse environmental adaptation strategies were used by the compared robots: ANYmal relied on precise sensing, planning, and control algorithms; M4 exhibited locomotion plasticity and had the capability to fly for short periods; ART applied adaptive morphogenesis for transitioning between land and water. Our robot optimized navigation and energy usage through coordinated

Table 1. Comparative analysis of robotic locomotion performance in diverse terrains. Side-by-side comparison of nonportable and portable field robots, including ANYmal, M4, ART, and our GOAT, highlighting key performance metrics, such as distance per charge, CoT, weight, and maximum velocity in both terrestrial and aquatic locomotion, as well as capabilities in environmental adaptation.

		Field robots (>10 kg)	**Portable field robots (<10 kg)**		
		ANYmal (*53*)	**M4 (*28*)**	**ART (*45*)**	**GOAT (ours)**
Terrestrial locomotion	Distance per charge (km)	2.2	0.24–2.5*	Tethered	2.5 (rolling) + 2 (driving) = 4.5
	Cost of transport	1.2	2.6–27.0*	10.6 to 30.0	0.1 (rolling) 0.8 (driving)
	Weight (kg)	30	5.6	9	2.8
	Payload (kg)	10	1.0*	No data	1.6
	Max. slope climbing (°)	21	45	No data	33
	Max. velocity (m/s)	1.2	0.7*	0.04	3.8 (rolling) 2.4 (driving)
	Max. drop height (m)	No data	No data	No data	10
Aquatic locomotion	Distance per charge (km)	Infeasible	Infeasible	Tethered	2
	Cost of transport			3.0–4.3	0.9
	Max. velocity (m/s)			0.09	1.2
Environmental adaptation	Strategy	Planning and control	Locomotion plasticity	Adaptive morphogenesis	Active reconfiguration and passive adaptation

*Estimated values, as extracted from raw data.

interactions with its environment by leveraging the passive properties of its compliant structure and actively reconfiguring its morphology under the influence of environmental stimuli.

DISCUSSION

In this work, we present a robot that is capable of active morphological reconfiguration and passively adapting to its environment. The bioinspired morphological reconfiguration enables different locomotion modalities, including driving, swimming, and rolling. Moreover, the robot can dynamically reconfigure its shape while in motion, for example, when rolling, allowing it to adapt instantaneously to changing paths and terrains. The compliance of the robot's structure offers local adaptation to obstacles in highly unstructured and uncertain environments such that complex terrains can be covered autonomously with minimal sensing and path planning. Furthermore, in different morphological configurations, the efficiency, feasible paths, and velocity of the robot are varied, opening up a wider range of environments and terrains for navigation. In doing so, with GOAT, we demonstrated kilometer-long distances of efficient travel across many different challenging terrains. The integration of active reconfiguration with structural compliance, as demonstrated in this work, offers the potential to substantially enhance the ability of future robots to efficiently and autonomously navigate complex and challenging environments.

To increase the robot's autonomy, future research in path planning should focus on creating algorithms that account for the unique capabilities of reconfigurable, compliant robots. Such algorithms should use a priori available information, such as topographic maps, to plan paths that leverage the varied abilities of these robots. Planned paths should include shape reconfigurations during rolling and actively leverage environmental features through actions like falling. The robot's compliant properties and its capacity for dynamic reconfiguration should also be integrated and leveraged by path-following controllers during autonomous navigation for increased performance and robustness. These algorithms could distribute the planning process and offload some computational tasks to the robot's physical form, enhancing the robot's efficiency and ability to follow more complex trajectories (*54*).

The proposed robot design shows promise for physical scalability, both larger and smaller, by adjusting the torsional and bending stiffness of the rods used. The payload capacity can be substantially enhanced by constructing the frame using rods or strips, with customized sections and reinforcements (*55*), and using materials with varying stiffness or structures for controllable stiffness (*56*). Adjusting the stiffness and scale of the frame allows for the exploration of the trade-off between payload capacity and compliance, which in turn influences the robot's morphing process, locomotion performance, and robustness. Optimal compliance not only is linked to the robot's design but also depends on environmental factors such as terrain type, obstacle height, and slope inclination. Computational design could be leveraged to optimize design parameters of the frame, such as scale and stiffness, or of the wheels, such as the number of spokes and their stiffness, for specific environments. The use of elastic fiberglass rods, winch-driven tendons, and electric motors provides a scalable fabrication method for morphing robots. Using these widely available materials allows for rapid design iterations and scalability. This approach could lead to a new generation of elastic, reconfigurable robots that combine structural compliance with active, dynamic, and substantial reconfiguration, capable of robustly navigating complex natural terrains with unprecedented versatility.

Harnessing a combination of passive adaptation and active morphological reconfiguration, the next generation of compliant robots could surpass nature's versatility. By varying their shape while in motion, these robots can dynamically adjust to environmental changes in real time. The potential for these robots to swiftly deploy into uncharted terrains with minimal perception and planning systems substantially enhances their applicability, turning environmental challenges into computational assets in the near future.

MATERIALS AND METHODS

Morphologically reconfigurable frame design

The robot's frame was constructed from four straight fiberglass rods, each 2 m in length and 5 mm in diameter. Fiberglass rods provide a high strength-to-weight ratio and can show substantial elastic deformation before permanent deformation or breakage occurs (*57*). The fiberglass rods were rigidly connected to form two fiberglass rings with a circumference of 4 m each. The two circles were stacked and connected at eight equidistant points on the circumference of each circle. Four of these joints connected both circles with an angle between them. They served as mounting points for the tendons and allowed the structure to bend and fold. Four others were rigid connections and enforced the convex symmetrical lens structure that allowed unambiguous morphological reconfiguration into a sphere and provided mounting points for the wheels. Each rigid connector was composed of two chevrons, the ends of which were attached to both circles using fixed T joints. Each chevron was formed by two 8-cm-long fiberglass rods that were connected in the middle by a fixed 3D-printed connector with an opening angle of 120°. This combination of rigid connections that enforced geometry in the frame enabled morphological reconfiguration.

Four motors were mounted to the fixed middle joints of each rigid connector's chevrons. The motors were waterproof and could supply 45 kg cm^{-1} of torque. Each motor drove a rimless wheel, which was fabricated from a central 3D-printed hub that held 10 spokes. The spokes were 25 cm long and made from 8-mm-thick fiberglass rods. The number and stiffness of the spokes were chosen heuristically, with 10 relatively stiff spokes providing a good balance between smooth motion and traction across various terrains. The spoke length was chosen to be as large as possible without intersecting or touching the robot's frame when rotating.

A waterproof payload in the middle of the frame was connected to the frame of the robot by two tendons from 0.6-mm braided polyethylene fishing line. The tendons spanned orthogonally over the frame, with one tendon running above and the other below the central payload. Each tendon was guided from the central payload through an eyelet on one connector of the robot frame to an eyelet on the diametrically opposite connector and back to the central payload, where they were connected to two electric winches. These two winches could each produce 40 kg cm^{-1} of torque and enabled the lengths of each of the tendons to be independently controlled. Both winches were retrofitted with encoders to measure the absolute angular position of their spools. Under slight tension, the two tendons held the payload of the robot in its center. Under higher tension, the tendons caused the robot's frame to deform. This property was key to enabling the robot to actively reconfigure its morphology.

Modeling morphological reconfiguration

The role of modeling and simulation was twofold: first, to optimize the geometry of the robot for spherical reconfiguration and, second, to analyze the robot's stability in different reconfigured states. Typically, models for simulating compliant morphing structures and robotic bodies are based on deformation parameters, such as piecewise constant curvature or piecewise constant strain. However, these models are suited for the forward simulation of slender structures, such as soft continuum robot arms. Our robot was constructed from elastic rods capable of large deformations and subject to complex loading conditions, so these models were not appropriate. Instead, we developed a modeling approach based on ANCF (*51*, *58*), which accurately predicted 3D deformations besides ensuring computational efficiency. This approach was used to simulate the 3D shape of the deformed robot with different rod geometries undergoing displacement from the two winch-driven tendons. In addition to the 3D shape, three other key metrics were determined: the robot's flexural rigidity, torsional rigidity, and elastic potential energy. The flexural rigidity and the nominal energy density distributed through the frame were important to assess the energy required by the winches to deform the structure and the forces in the tendons. These needed to be kept low so that the reconfiguration remained within the capabilities of the winches. Torsional stiffness was key to understanding the robot's stability during its reconfiguration process. A joint's torsional stiffness dropping below zero could lead to undesirable and unstable twisting movements.

ANCF modeling for elastic rods

We briefly introduce our adapted ANCF modeling method for elastic rods. An elastic rod was modeled as n discrete elements, described by $n + 1$ nodes along its axial center line; this reference frame and parameterization is detailed in Supplementary Materials and Methods. Given this parameterization and the absolute nodal coordinates (which relate to the central axis of the rod), we obtained the displacement field for the entire rod structure. The axial Green strain ε, bending curvature k_b, and torsion k_t were calculated from the displacement field at each node to obtain the energy density distribution along the rod. Integrating along the length of the rod structure allowed us to obtain its elastic potential energy. The generalized nodal force was obtained from the partial differential of the elastic potential energy across the nodal coordinates. From this, we solved a pseudodynamic equation to resolve the quasistatic state that is the configuration of the central axis of the rod. This formed the basis of the simulation. More information can be found in the Quasistatic solution section in Supplementary Materials and Methods.

Robot simulation

The ANCF method was used to build a complete simulation for the robot. This was used to simulate different geometries of robot structures undergoing different tendon displacements as shown in Fig. 2B (ii). The 3D configuration of the robot could, in turn, be used to obtain the tendon forces (Fig. 2B) from the nodal forces in a quasistatic state based on the balanced pseudodynamic equation of the structure (eq. S10 in Supplementary Materials and Methods). The tendon forces provided insight into the energetics and stability of the robot. To simulate different robot geometries undergoing different forms of reconfiguration, such as in-plane or out-of-plane reconfiguration, we had to identify the necessary boundary conditions and connection constraints for each scenario.

Quarter-robot simulation: Dual-symmetric, no-twisting configurations

For in-plane and out-of-plane deformation, when no twisting occurred, there were two planes of symmetry (X-Z and Y-Z) in the robot, so only a quarter had to be simulated; the definition of these axes and planes is given in figs. S2 to S4. For each of the three robot structures evaluated (rod, band, and lens), their coordinate system and constraints had to be designed appropriately.

Single rod. For in-plane deformation of a single-rod structure robot (Fig. 2B, ii), we modeled it as a quarter of a circular rod where one end was fully constrained and the other was moved in the x axis by the given tendon displacement (table S2). For out-of-plane deformation, one end was moved by the given tendon placement in the y axis, and the other end was free to move in the z axis (table S3).

Band. The band structure was simulated as two circular rods connected with orthogonal transversal rods. To represent these physical constraints, we introduced a new node, which was equidistant between the two connected rods and rigidly constrained to lie between them (fig. S3A), as detailed in the "Band structure" section in Supplementary Materials and Methods. The boundary conditions given for the single rod structure were also applied to this new node (fig. S3).

Lens. To represent the structure of the lens with the crossed points at the end of each quarter, we introduced a new node that was rigidly constrained to the two rods but had the average orientation of the two (see the "Lens structure" section in Supplementary Materials and Methods). The standard boundaries as detailed above could then be applied to these new nodes (fig. S4).

Half-robot simulation: Torsional stiffness

Under most tendon displacements, the single rod circle or lens structures had a stable dual-symmetrical configuration. However, when the ratio between the longer (major) axis and the shorter (minor) axis was too high, the structure became unstable and twisted into an antisymmetric complex configuration to reach a lower elastic potential energy state. This twisting was undesirable because it led to a "tent-folding"–like deformation from which it could not easily be recovered. To analyze the occurrence of this twisting, the torsional stiffness of the pivot point along the minor axis was predicted and used as an indication of the stability of the structure.

The simulation of the torsional stiffness was performed using a half-circle structure spanning the minor axis of the robot (fig. S5), where the position and local frame of the two end points of this half circle were coupled on the basis of its antisymmetrical geometry (see table S6). The middle point of the half rod was constrained in the z axis. To evaluate the elastic potential energy with increasing torsional deformation, the x axis of the local frame was moved stepwise in the X-Y plane, simulating changing tendon lengths. More details about boundary conditions are given in table S6 and the "Stability analysis" section in Supplementary Materials and Methods.

Using this half-circle simulation, the potential elastic energy U_E and the twisting angle θ of the structure were determined. The relationship between these was captured with a higher-order polynomial, where the concavity determined the stability of the structure (figs. S6 and S7). Specifically, the second derivative of this function, $\frac{\delta U_E{}^2}{\delta\theta^2}|_{\theta=0}$, defined the torsional stiffness along the minor axis of the robot and was used as an indication of the structural stability. This was calculated by fitting a function between U_E and θ for only a small range of θ between 0° and 2°. This torsional stiffness was computed for different in-plane and out-of-plane configurations and mapped back to the tendon lengths to enable the stability analysis given in Fig. 2C.

As shown in Fig. 2C, this unstable twisting behavior could emerge from different tendon configurations and could lead to in-plane or out-of-plane twisting. The occurrence of these two different twisting behaviors is described in the following paragraphs.

In-plane twisting. In-plane twisting occurred when starting from an in-plane configuration with a high aspect ratio, meaning that the tendon in the x axis was short. When this was extreme, the robot structure took on the lowest energy state, which introduced twisting with two antisymmetrical axes (z axis and y axis), as shown in fig. S6. The shorter the x axis tendon, the greater the twisting angle at the midpoint and the lower the stability. As such, its stability decreased with the shortness of the distance along the x axis (the minor axis).

Out-of-plane twisting. An out-of-plane configuration emerged when there was an unstable in-plane configuration that had a tendency to twist, followed by a tendon displacement that decreased the distance along the y axis (the major axis). Here, its stable twisting angle would decrease until the dual-symmetrical configuration reached the lowest energy state, as shown in fig. S7. This meant that configurations with a shorter distance along the y axis (the major axis) showed higher stability in the dual-symmetrical configuration.

Full-robot simulation: Tent folding deformation

Although simulation of the half circle of the robot was used to identify when twisting happened, by simulating the whole robot structure, we could analyze the full 3D-folded unstable out-of-plane configuration (fig. S8). The boundary conditions for this full circle of the structure are defined in table S6. For this simulation, the start and end points of the rod were the same and fully coupled. The distance between the one-quarter point and three-quarter point along the circular rod was fixed to represent the constant length of tendon 1. More details can be found in the "Stability analysis" section in Supplementary Materials and Methods. When simulating the reduction in the length of tendon 2, which was modeled as reduced distance along the y axis, the unstable dual-symmetrical configuration resulted in the tent folding configuration as shown in fig. S8 and movie S9.

Electronics

All actuators, sensors, computing, and power electronics, except the motors that drove the robot's four wheels, were housed within the robot's central payload. A diagram of the robot's electronic components is shown in fig. S11. The central payload served as a hub for both power and data communication. The wheel motors received their power through cable conduits that run from this central payload. These conduits extended from the motors, running along the robot's frame and tendons, and converged at the central payload. The robot's actuation system consisted of its four wheel motors and the two winch motors. All motors were compatible with direct power supply from three cell lithium polymer (3S LiPo) batteries. Typically, the robot was powered with a 1600-mAh 3S LiPo battery because this battery provided a good trade-off between operational weight and the robot's designated operation period of approximately 30 min of continuous driving or 2 hours of rolling. Power management, crucial for the robot's functionality, was handled by a Holybro PM02D power module. This board regulated the battery's output, stepping down the voltage from 12 to 5 V, ensuring efficient energy distribution to power the robot's central processing unit and its sensors.

Sensors

The robot's central processing unit, a Raspberry Pi 5 (8 GB), established connectivity with various peripheral electronics essential for operation via the Inter-Integrated Circuit (I2C) protocol. This included an Adafruit PCA9685 16-channel pulse-width modulation (PWM)/servo driver, which generated PWM signals for controlling the robot's winches and motors. Angular measurements of the winches were captured by two AMS AS5048B rotary position sensors. Precise acceleration, angular rate, and magnetic field measurements were obtained by an Adafruit LSM6DSOX + LIS3MDL 9–degrees-of-freedom (DoF) IMU. Last, a Texas Instruments INA220 current and power monitor, which was integrated into the power module, tracked the robot's power consumption metrics. For high-precision location tracking, the system integrated a Septentrio MosaicHat connected to a lightweight ArduSimple Helical GNSS Tripleband + L-band antenna. This setup enabled the acquisition of GNSS measurements at a rate of 100 Hz. Real-time kinematic corrections were streamed over the cellular network from the swipos-GIS/GEO service, enabling localization with sub-centimeter precision. The Raspberry Pi connected to the cellular network via a Wi-Fi connection to a TP-Link M7650 mobile Wi-Fi router, which was likewise housed in the robot's payload.

Software and data recording

The software framework driving the robot was executed on its onboard computer. During operation, the onboard computer and connected sensors consumed approximately 800 mA. The robot's software framework followed a modular approach, with each module developed in compliance with the Robot Operating System (ROS 2) framework (*59*). Despite the availability of many out-of-the-box packages, our project necessitated the development of modules tailored to the robot's functions, such as drivers for the Adafruit PCA9685 PWM/Servo driver. These newly developed modules were released as open-source packages with a permissive license under the ROSbloX project (*60*). The implemented software framework not only drove the robot's core functionalities but also ensured efficient onboard data recording and management during operation and allowed monitoring the state of the robot through a web interface.

State estimation and sensor fusion

The robot's raw sensor measurement streams were recorded for postprocessing and data analysis. Further, these measurements were used for automatic control of the robot and autonomous navigation. However, they were generally subject to noise and not suitable for controlling the robot without using modeling, state estimation, and sensor fusion. The robot's state was divided into two parts: its morphological state, a function of its tendon lengths; and its position and orientation with respect to an inertial frame, that is, its pose (6 DoF) with respect to a fixed north-east-down (NED) coordinate frame and its change over time. Neither its morphological state nor its global pose could be measured directly and had to be estimated. Both winches were retrofitted with rotary position sensors that measured rotations of the spools that hold the tendons. The encoder measurements were integrated to obtain the absolute number of turns for each spool, ψ. Following (*61*), the tendons winding up on the spool were modeled as an Archimedean spiral, and the length of each tendon was estimated as

$$\hat{l}_{1,2} := \pi\left(d_{\max} - 2\delta_{\mathbf{r}}\psi\right) \tag{1}$$

whereby $d_{\max}$ and δ_r correspond to the diameter of the spool when the whole tendon was wound up and the radial decay rate. Parameters $d_{\max}$ and δ_r were determined in a one-time calibration. The estimated tendon lengths $\hat{l}_{1,2}$ were linked to the robot's morphology as described in the "Modeling morphological reconfiguration" section. The robot's body was fully symmetric. Each side could be defined as its front, back, left, or right side. Equally, the robot top and bottom were the same. However, for autonomous navigation, a coordinate frame was fixed to its central payload, with its x axis following one tendon, its y axis the second tendon, and the z axis completing a right-hand coordinate system. In the following, we refer to the direction of the x axis as forward, the y axis direction as left, and z axis direction as top. An inertial coordinate frame following an NED convention was introduced and served as a global reference. To estimate the robot's absolute orientation, in terms of its roll, pitch, and yaw angles, with respect to the inertial frame, we used a complementary filter (*62*) that fused angular velocities, linear accelerations, and magnetic field direction measurements of the IMU at 20 Hz. The measured angular velocities and linear accelerations, the robot's estimated absolute orientation in the inertial frame, and GNSS measurements were fused using an unscented Kalman filter (*63*) to estimate the robot's 6-DoF pose in the inertial frame at 20 Hz. The applied filter (*64*) estimated a fifteen-dimensional state, with nine states linked to the robot's 3D position, linear velocity, and acceleration and six states representing its 3D orientation and angular velocity. The sensor fusion with GNSS fusion was only applicable in outdoor environments. For laboratory experiments, pose measurements at 120 Hz streamed from an OptiTrack Motion Capture system served as ground truth.

Control, autonomy, and path planning

Automatic control was implemented to control the robot's electric winches and wheel motors to enable teleoperation, autonomous morphological reconfiguration, and navigation.

Morphological reconfiguration

The electric winches controlled the tendon lengths. A cascaded control scheme was applied to vary the tendon lengths and allowed for controlled reconfiguration of the robot's morphology to either take on a spherical shape or a shape suitable for driving, as shown in Fig. 2A. The cascaded control scheme is visualized in fig. S12. The length of each tendon was controlled individually to follow a set reference length. A proportional gain controller was implemented to control the current tendon lengths $l_{\text{est},n}$ to follow the reference length, $l_{ref,n}$,

$$u_{\text{motor},n} = P_{\text{gain}}\left(\left(l_{\text{ref},n} - \hat{l}_n\right) \text{ with } n \in [1,2]\right. \tag{2}$$

The controller's gain, P_{gain}, was determined experimentally. When a tuple of reference lengths, $T_{\text{ref}} := \left(l_{\text{ref},1}, l_{\text{ref},2}\right)$, was given to the winch controllers, both winches controlled the tendons to the respective reference lengths independently. For automatic morphological reconfiguration, a trajectory controller was implemented that enabled synchronized control of both tendons. The morphological trajectory controller took as input a morphological reconfiguration trajectory consisting of a series of tuples of K reference lengths, $T_{\text{ref},1} \cdot \ldots T_{\text{ref},K}$. Each tuple was commanded to the low-level tendon controllers sequentially by the trajectory controller, whereby consecutive tuples were executed only if the prior tuple had been successfully reached. The execution of these morphological trajectories allowed precise control of the robot's morphological state and enabled the automatic execution of the morphing trajectories in the robot's morphological reconfiguration space as shown in Fig. 2.

Two morphological states of the robot and the transition between these states were of particular interest because they enabled the robot to navigate efficiently and robustly in outdoor environments. These states were its flat configuration, which enabled the robot to drive using its wheels, and its spherical, curled-up shape, in which the robot's payload and wheels were protected and it was able to roll. These configurations are indicated in the morphological reconfiguration diagram in Fig. 2C by markers 2 (rover configuration) and 4 (spherical configuration).

To transition from a flat to a spherical configuration and vice versa, a morphological trajectory was introduced. This trajectory steered the tendons through an intermediate configuration, labeled as point 3 in the diagram in Fig. 2C. Introducing this trajectory ensured stable morphological reconfiguration and avoided the twisting of the robot indicated by the blue areas in the diagram in Fig. 2C.

The morphological reconfiguration from rover to spherical shape was only one of the robot's features enabled by the morphological trajectory controller. Further morphological reconfigurations included in-plane reconfiguration such as elongation of the robot's frame, which made it more suitable for fast forward motion or to a more circular shape suitable for efficient and stable turning. Last, the morphology controller allowed the robot to change its center of gravity when in a spherical (and almost spherical) shape by altering the position of the payload suspended in the robot's frame. The payload made up nearly two-thirds of the robot's mass. Changing its location inside the robot's frame shifted the robot's center of gravity outside its support polygon and initiated rolling motion even on flat ground, as shown in Fig. 4D.

Low-level driving control

In its flat configuration, the robot resembled a four-wheeled, skid-steered, mobile robot whose movement and direction were controllable by differentially driving the wheels on either side of the robot. The left and right sides of the robot were defined as the robot's frame and wheels, which were located to the left and right sides of the longer tendon. The wheels on each side moved at the same speed. When the wheels on both sides were driven at the same speed and direction, the robot moved forward or backward in a straight line. Steering was achieved by varying the relative speeds of the wheels on either side, causing the robot to skid or slide as it turned. To control the skid-steered robot, input linear velocity, v, and angular velocity, ω, were translated into wheel velocities by a low-level driving controller. The low-level driving controller computed velocities of the left and right wheels v_L and v_R as follows

$$v_L = v - \frac{\omega d}{2} \tag{3}$$

and

$$v_R = v + \frac{\omega d}{2} \tag{4}$$

where d is the robot's track width. This method effectively converted the desired motion into differential wheel speeds, enabling precise maneuvering of the robot.

Autonomous navigation

The robot could be operated remotely and autonomously. Remote control was facilitated through a Sony Dualshock PlayStation 4 game pad, which wirelessly connected to the robot's Raspberry Pi via Bluetooth. For autonomous navigation, the robot leveraged its morphological reconfiguration capability to alternate between rolling and driving modes. We augmented traditional navigation techniques with innovative strategies to fully use this feature. On slopes, rolling was preferred for its safety and energy efficiency. Hence, it was favorable for the robot to curl up and roll where feasible, only reverting to its rover configuration when rolling became impractical to reach its destination.

Three distinct navigation strategies were implemented using the ROS 2 Navigation2 (Nav2) (*65*) framework to autonomously move toward predefined waypoints. Nav2 is a production-grade navigation framework designed for building highly reliable autonomous systems (*66*). For each navigation strategy, a high-level path planning algorithm continuously computed the shortest path between the robot's current location and a target waypoint. Once a path was planned, a low-level controller computed motor commands to follow the planned path using the dynamic window approach (*67*). The controller used feedback from the robot's sensors to dynamically adjust the robot's speed and direction. The implemented navigation strategies differed in the integration of different high-level behaviors.

We refer to the three implemented navigation strategies as "basic navigation," "reflexive approach," and "trajectory-informed strategy." The basic navigation strategy used the default navigation behavior for skid-steered rovers implemented in Nav2. For simplicity, recovery strategies as navigational behavior were disabled. The reflexive approach combined rolling and driving. Wherever rolling was possible, the robot changed to its spherical configuration and started rolling until it stopped automatically, either because of an obstacle or upon reaching flat ground. It then morphed to its rover configuration and drove toward the goal. The trajectory-informed strategy incorporated information about the robot's prior trajectory. When rolling was feasible, the robot reconfigured into a sphere and rolled toward the target waypoint. It actively stopped rolling and unfolded when closest to its destination.

These strategies are delineated and their performance evaluated in Figs. 5 and 6, illustrating the effectiveness of each approach. A schematic visualization is shown in fig. S13. Currently, our strategies do not incorporate prior topographical data into path planning, indicating a potential area for future refinement.

Statistical analysis

Figure 3 (A and B) visualizes the robot's success rate when driving and morphing over obstacles, respectively, when squeezing through gaps. For the five step heights and seven gap widths, the corresponding bars show the success rate as a percentage of 12 consecutive trials.

Figure 4 (B and C) shows the influence of the aspect ratio on the velocity and positional error, respectively, and the angular velocity and turning radius of the robot. For each of the five evaluated aspect ratios per plot, mean and SD were calculated from six trials.

Supplementary Materials

The PDF file includes:

Materials and Methods
Figs. S1 to S14
Tables S1 to S7
Legends for movies S1 to S9

Other Supplementary Material for this manuscript includes the following:

Movies S1 to S9

REFERENCES AND NOTES

1. P. Ramdya, A. J. Ijspeert, The neuromechanics of animal locomotion: From biology to robotics and back. *Sci. Robot.* **8**, eadg0279 (2023).
2. J. Lee, J. Hwangbo, L. Wellhausen, V. Koltun, M. Hutter, Learning quadrupedal locomotion over challenging terrain. *Sci. Robot.* **5**, eabc5986 (2020).
3. T. Miki, J. Lee, J. Hwangbo, L. Wellhausen, V. Koltun, M. Hutter, Learning robust perceptive locomotion for quadrupedal robots in the wild. *Sci. Robot.* **7**, eabk2822 (2022).
4. A. Torres-Pardo, D. Pinto-Fernández, M. Garabini, F. Angelini, D. Rodriguez-Cianca, S. Massardi, J. Tornero, J. C. Moreno, D. Torricelli, Legged locomotion over irregular terrains: State of the art of human and robot performance. *Bioinspir. Biomim.* **17**, 061002 (2022).
5. F. Angelini, P. Angelini, C. Angiolini, S. Bagella, F. Bonomo, M. Caccianiga, C. Della Santina, D. Gigante, M. Hutter, T. Nanayakkara, P. Remagnino, D. Torricelli, M. Garabini, Robotic monitoring of habitats: The natural intelligence approach. *IEEE Access* **11**, 72575–72591 (2023).
6. M. Dunbabin, L. Marques, Robots for environmental monitoring: Significant advancements and applications. *IEEE Robot. Autom. Mag.* **19**, 24–39 (2012).
7. A. King, Technology: The future of agriculture. *Nature* **544**, S21–S23 (2017).
8. P. E. Glick, J. B. Balaram, M. R. Davidson, E. Lyons, M. T. Tolley, The role of low-cost robots in the future of spaceflight. *Sci. Robot.* **9**, eadl1995 (2024).
9. J. Delmerico, S. Mintchev, A. Giusti, B. Gromov, K. Melo, T. Horvat, C. Cadena, M. Hutter, A. Ijspeert, D. Floreano, L. M. Gambardella, R. Siegwart, D. Scaramuzza, The current state and future outlook of rescue robotics. *J. Field Rob.* **36**, 1171–1191 (2019).
10. C. Li, K. Lewis, The need for and feasibility of alternative ground robots to traverse sandy and rocky extraterrestrial terrain. *Adv. Intell. Syst.* **5**, 2100195 (2023).
11. H. Kalita, J. Thangavelautham, Exploration of extreme environments with current and emerging robot systems. *Curr. Robot. Rep.* **1**, 97–104 (2020).
12. F. Stella, J. Hughes, The science of soft robot design: A review of motivations, methods and enabling technologies. *Front. Robot. AI* **9**, 1059026 (2023).
13. S. Kim, C. Laschi, B. Trimmer, Soft robotics: A bioinspired evolution in robotics. *Trends Biotechnol.* **31**, 287–294 (2013).
14. K. Jayaram, R. J. Full, Cockroaches traverse crevices, crawl rapidly in confined spaces, and inspire a soft, legged robot. *Proc. Natl. Acad. Sci. U.S.A.* **113**, E950–E957 (2016).
15. D. Morgan, U. Proske, D. Warren, Measurements of muscle stiffness and the mechanism of elastic storage of energy in hopping kangaroos. *J. Physiol.* **282**, 253–261 (1978).
16. W. M. Kier, M. P. Stella, The arrangement and function of octopus arm musculature and connective tissue. *J. Morphol.* **268**, 831–843 (2007).
17. K. Schmidt-Nielsen, *Animal Physiology: Adaptation and Environment* (Cambridge Univ. Press, 1997), vol. 359.
18. A. Berger, L. M. F. Barthel, W. Rast, H. Hofer, P. Gras, Urban hedgehog behavioural responses to temporary habitat disturbance versus permanent fragmentation. *Animals* **10**, 2109 (2020).
19. C. Stapp, "Defensive diversity: Factors influencing the interspecific variation in the armor of armadillos (*Cingulata*)," thesis, California State University, Long Beach (2022).
20. I. H. Tuf, B. Ďurajková, Antipredatory strategies of terrestrial isopods. *ZooKeys* **1101**, 109–129 (2022).
21. N. Møbjerg, K. Halberg, A. Jørgensen, D. Persson, M. Bjørn, H. Ramløv, R. Kristensen, Survival in extreme environments–on the current knowledge of adaptations in tardigrades. *Acta Physiol.* **202**, 409–420 (2011).
22. S. R. Kundu, *Spider Evolution: Genetics, Behavior, and Ecological Influences* (Academic Press, 2021).
23. D. V. Baker, J. R. Withrow, C. S. Brown, K. G. Beck, Tumbling: Use of diffuse knapweed (*Centaurea diffusa*) to examine an understudied dispersal mechanism. *Invasive Plant Sci. Manag.* **3**, 301–309 (2010).
24. A. Rafsanjani, V. Brulé, T. L. Western, D. Pasini, Hydro-responsive curling of the resurrection plant *Selaginella lepidophylla*. *Sci. Rep.* **5**, 8064 (2015).
25. B. T. Wilcox, J. Joyce, M. D. Bartlett, Rapid and reversible morphing to enable multifunctionality in robots. *Adv. Intell. Syst.* **2025**, 2300694 (2025).
26. E. Gefen, D. Zarrouk, Flying STAR2, a hybrid flying driving robot with a clutch mechanism and energy optimization algorithm. *IEEE Access* **10**, 115491 (2022).
27. S. K. Mahmood, S. H. Bakhy, M. A. Tawfik, Propeller-type wall-climbing robots: A review, in *IOP Conference Series: Materials Science and Engineering* (IOP Publishing, 2021), vol. 1094, p. 012106.
28. E. Sihite, A. Kalantari, R. Nemovi, A. Ramezani, M. Gharib, Multi-modal mobility Morphobot (M4) with appendage repurposing for locomotion plasticity enhancement. *Nat. Commun.* **14**, 3323 (2023).
29. Y.-S. Kim, G.-P. Jung, H. Kim, K.-J. Cho, C.-N. Chu, Wheel transformer: A wheel-leg hybrid robot with passive transformable wheels. *IEEE Trans. Robot.* **30**, 1487–1498 (2014).
30. S. Iversen, J. Jouffroy, "Umbrella wheel — A stair-climbing and obstacle-handling wheel design concept," in *2017 International Conference on Advanced Mechatronic Systems (ICAMechS)* (IEEE, 2017), pp. 312–317.

31. T. Sun, X. Xiang, W. Su, H. Wu, Y. Song, A transformable wheel-legged mobile robot: Design, analysis and experiment. *Robot. Auton. Syst.* **98**, 30–41 (2017).
32. K. Shi, Z. Jiang, L. Ma, L. Qi, M. Jin, MTABot: An efficient morphable terrestrial-aerial robot with two transformable wheels. *IEEE Robot. Autom. Lett.* **9**, 1875–1882 (2024).
33. H. Banerjee, S. Kakde, H. Ren, "OrumBot: Origami-based deformable robot inspired by an umbrella structure," in *2018 IEEE International Conference on Robotics and Biomimetics (ROBIO)* (IEEE, 2018), pp. 910–915.
34. J. T. Karras, C. L. Fuller, K. C. Carpenter, A. Buscicchio, D. McKeeby, C. J. Norman, C. E. Parcheta, I. Davydychev, R. S. Fearing, "Pop-up mars rover with textile-enhanced rigid-flex PCB body," in *2017 IEEE International Conference on Robotics and Automation (ICRA)* (IEEE, 2017), pp. 5459–5466.
35. C. H. Belke, K. Holdcroft, A. Sigrist, J. Paik, Morphological flexibility in robotic systems through physical polygon meshing. *Nat. Mach. Intell.* **5**, 669 (2023).
36. J. Seo, J. Paik, M. Yim, Modular reconfigurable robotics. *Annu. Rev. Control Robot. Auton. Syst.* **2**, 63 (2019).
37. Y. Liu, Q. Bi, X. Yue, J. Wu, B. Yang, Y. Li, A review on tensegrity structures-based robots. *Mech. Mach. Theory* **168**, 104571 (2022).
38. N. S. Usevitch, Z. M. Hammond, M. Schwager, A. M. Okamura, E. W. Hawkes, S. Follmer, An untethered isoperimetric soft robot. *Sci. Robot.* **5**, eaaz0492 (2020).
39. M. Tolley, R. F. Shepherd, B. Mosadegh, K. C. Galloway, M. Wehner, M. Karpelson, R. J. Wood, G. M. Whitesides, A resilient, untethered soft robot. *Soft Robot.* **1**, 213–223 (2014).
40. D. Shah, B. Yang, S. Kriegman, M. Levin, J. Bongard, R. Kramer-Bottiglio, Shape changing robots: Bioinspiration, simulation, and physical realization. *Adv. Mater.* **33**, 2002882 (2021).
41. G. Dudek, P. Giguere, C. Prahacs, S. Saunderson, J. Sattar, L.-A. Torres-Mendez, M. Jenkin, A. German, A. Hogue, A. Ripsman, J. Zacher, E. Milio, H. Liu, P. Zhang, M. Buehler, C. Georgiades, AQUA: An amphibious autonomous robot. *Computer* **40**, 46–53 (2007).
42. R. Altendorfer, N. Moore, H. Komsuoglu, M. Buehler, H. B. Brown Jr., D. McMordie, U. Saranli, R. Full, D. E. Koditschek, RHex: A biologically inspired hexapod runner. *Auton. Robot.* **11**, 207–213 (2001).
43. B. B. Dey, S. Manjanna, G. Dudek, "Ninja legs: Amphibious one degree of freedom robotic legs," in *2013 IEEE/RSJ International Conference on Intelligent Robots and Syst. (IROS)* (IEEE, 2013), pp. 5622–5628.
44. J. Sun, E. Lerner, B. Tighe, C. Middlemist, J. Zhao, Embedded shape morphing for morphologically adaptive robots. *Nat. Comm.* **14**, 6023 (2023).
45. R. Baines, S. K. Patiballa, J. Booth, L. Ramirez, T. Sipple, A. Garcia, F. Fish, R. Kramer-Bottiglio, Multi-environment robotic transitions through adaptive morphogenesis. *Nature* **610**, 283–289 (2022).
46. N. Savage, Bioinspired robots walk, swim, slither and fly. *Nature Outlook: Robotics and Artificial Intelligence* (2022); 10.1038/d41586-022-03014-x.
47. A. Western, M. Haghshenas-Jaryani, M. Hassanalian, Golden wheel spider-inspired rolling robots for planetary exploration. *Acta Astronaut.* **204**, 34–48 (2023).
48. C. Dunning, R. Cervantes, L. Velasquez, A. Western, M. Sherman, M. Hassanalian, "Design and manufacturing of a bioinspired spider rolling robot for Mars exploration," in *AIAA Scitech 2021 Forum* (AIAA, 2021), p. 0958.
49. B. W. Mulvey, T. D. Lalitharatne, T. Nanayakkara, Deformobot: A bio-inspired deformable mobile robot for navigation among obstacles. *IEEE Robot. Autom. Lett.* **8**, 3828–3835 (2023).
50. R. Armour, K. Paskins, A. Bowyer, J. Vincent, W. Megill, R. Bomphrey, Jumping robots: A biomimetic solution to locomotion across rough terrain. *Bioinspir. Biomim.* **2**, S65–S82 (2007).
51. X. Huang, X. Zhu, G. Gu, Kinematic modeling and characterization of soft parallel robots. *IEEE Trans. Robot.* **38**, 3792–3806 (2022).
52. L. Lu, S. Leanza, J. Dai, X. Sun, R. R. Zhao, Easy snap-folding of hexagonal ring origami by geometric modifications. *J. Mech. Phys. Solids* **171**, 105142 (2023).
53. M. Hutter, C. Gehring, D. Jud, A. Lauber, C. D. Bellicoso, V. Tsounis, J. Hwangbo, K. Bodie, P. Fankhauser, M. Bloesch, R. Diethelm, S. Bachmann, A. Melzer, M. Hoepflinger, "ANYmal - a highly mobile and dynamic quadrupedal robot," in *2016 IEEE/RSJ International Conference on Intelligent Robots and Systems (IROS)* (IEEE, 2016), pp. 38–44.
54. Y. I. Sobolev, R. Dong, T. Tlusty, J.-P. Eckmann, S. Granick, B. A. Grzybowski, Solid-body trajectoids shaped to roll along desired pathways. *Nature* **620**, 310–315 (2023).
55. J. Mlýnek, M. Petrů, T. Martinec, S. S. R. Koloor, Fabrication of high-quality polymer composite frame by a new method of fiber winding process. *Polymers* **12**, 1037 (2020).
56. O. Weeger, Y. S. B. Kang, S.-K. Yeung, M. L. Dunn, Optimal design and manufacture of active rod structures with spatially variable materials. *3D Print. Addit. Manuf.* **3**, 204 (2016).
57. M. Esrin, J. Gartner, Test method for evaluation of the resistance of fiberglass rods to combined mechanical and chemical stress. *IEEE Trans. Power Appar. Syst.* **PAS-103**, 2741–2745 (1984).
58. A. A. Shabana, R. Y. Yakoub, Three dimensional absolute nodal coordinate formulation for beam elements: Theory. *J. Mech. Des.* **123**, 606–613 (2001).
59. S. Macenski, T. Foote, B. Gerkey, C. Lalancette, W. Woodall, Robot Operating System 2: Design, architecture, and uses in the wild. *Sci. Robot.* **7**, eabm6074 (2022).
60. M. Polzin, ROSbloX: Accelerating robot software development with modular ROS building blocks (2024); https://rosblox.github.io/.
61. P. McGarey, M. Polzin, T. D. Barfoot, "Falling in line: Visual route following on extreme terrain for a tethered mobile robot," in *2017 IEEE International Conference on Robotics and Automation (ICRA)* (IEEE, 2017), pp. 2027–2034.
62. R. G. Valenti, I. Dryanovski, J. Xiao, Keeping a good attitude: A quaternion-based orientation filter for IMUs and MARGs. *Sensors* **15**, 19302 (2015).
63. E. Wan, R. Van Der Merwe, "The unscented Kalman filter for nonlinear estimation," in *Proceedings of the IEEE 2000 Adaptive Systems for Signal Processing, Communications, and Control Symposium* (IEEE, 2000), pp. 153–158.
64. T. Moore, D. Stouch, "A generalized extended Kalman filter implementation for the Robot Operating System" in *Intelligent Autonomous Systems 13*, E. Menegatti, N. Michael, K. Berns, H. Yamaguchi, Eds. (Springer International Publishing, 2016), pp. 335–348.
65. S. Macenski, F. Martin, R. White, J. G. Clavero, "The Marathon 2: A navigation system," in *2020 IEEE/RSJ International Conference on Intelligent Robots and Systems (IROS)* (IEEE, 2020), pp. 2718–2725.
66. S. Macenski, T. Moore, D. V. Lu, A. Merzlyakov, M. Ferguson, From the desks of ROS maintainers: A survey of modern & capable mobile robotics algorithms in the robot operating system 2. *Robot. Auton. Syst.* **168**, 104493 (2023).
67. D. Fox, W. Burgard, S. Thrun, The dynamic window approach to collision avoidance. *IEEE Robot. Autom. Mag.* **4**, 23–33 (1997).
68. Masteraah, Steppenschuppentier1a.jpg (2004); https://commons.wikimedia.org/wiki/File:Steppenschuppentier1a.jpg.
69. Masteraah, Steppenschuppentier2.jpg (2004); https://commons.wikimedia.org/wiki/File:Steppenschuppentier2.jpg.
70. I. Rechenberg, Cebrennus_rechenbergi_1.jpg (2014); https://commons.wikimedia.org/wiki/File:Cebrennus_rechenbergi_1.jpg.
71. L. Worch, White_lady.jpg (2016); https://commons.wikimedia.org/wiki/File:White_lady.jpg.

Acknowledgments: We thank members of the CREATE Lab, especially K. Junge, for assistance with experiments, practical advice, and support. **Funding:** This work was supported by the Swiss Polar Institute (TEG-2023-001), CROSS, and E4S. **Author contributions:** M.P. conceived the original idea, led the system design and development, and conducted experiments to validate the project. Q.G. was responsible for the mathematical analysis, focusing on simulations and modeling to underpin the project's theoretical framework. J.H. supervised the research, supporting the project's execution and development. All authors contributed to writing the manuscript. **Competing interests:** M.P. and J.H. hold a patent on the design of the robot structure. All other authors declare that they have no competing interests. **Data and materials availability:** All data needed to evaluate the conclusions in the paper are present in the paper or the Supplementary Materials. The software developed in this study has been deposited in a public database and is available at https://doi.org/10.5281/zenodo.13964001 and https://doi.org/10.5281/zenodo.13964003.

Submitted 5 April 2024
Accepted 28 January 2025
Published 26 February 2025
10.1126/scirobotics.adp6419

Science Robotics

Robotic locomotion through active and passive morphological adaptation in extreme outdoor environments

Max Polzin, Qinghua Guan, and Josie Hughes

Sci. Robot. **10** (99), eadp6419. DOI: 10.1126/scirobotics.adp6419

Science Robotics (ISSN 2470-9476) is published by the American Association for the Advancement of Science. 1200 New York Avenue NW, Washington, DC 20005. The title *Science Robotics* is a registered trademark of AAAS.